Available online at www.sciencedirect.com
SCIENCE DIRECT®

Journal of the European Ceramic Society 24 (2004) 345–361

www.elsevier.com/locate/jeurceramsoc

Numerical simulation of solid state sintering; model and application

Torsten Kraft, Hermann Riedel*

Fraunhofer-Institute for Materials Mechanics, Wöhlerstrasse 11, D-79108 Freiburg, Germany

Abstract

A comprehensive model for solid state sintering is presented which combines several previous models for partial aspects of sintering and grain coarsening. Some additional aspects are discussed and the model is extended for external loads several times higher than the sintering stress. Model parameters for a SiC powder are presented. For a face seal made of SiC uniaxial die compaction is simulated and different green density distributions after compaction are obtained for two different pressing schedules. Next, the sintering behavior is simulated using these density distributions as initial conditions. The resulting distortions of the face seal differ significantly for the two pressing schedules. For a special element with average green density the predictions of the sintering model are investigated in more detail. Finally, the shape predictions of the model are compared with a simplified model for solid state sintering.

Keywords: Pressing; SiC; Sintering; Simulation; Wear parts

1. Introduction

Nearly all production processes of ceramic parts include a sintering step at high temperature, which influences most material and overall part properties. Therefore, investigating sintering in detail is a necessity if industrial production processes have to be further optimized as is a steadily increasing economical demand. But, application of sintering models to industrial processing to predict densification and microstructural evolution failed to be useful for a long time. Reliable quantitative predictions for the effects of varying composition and particle shape, for varying sintering and pre-sintering conditions, and for changes of the shape of the sintered part were not possible. This, among other deficiencies, made the derivation of analytical equations as well as early numerical approaches an interesting exercise from a scientific point of view, yet unhelpful with respect to technical exploitation. The success of present approaches indicates that the situation may have changed. Final shapes of complex powder metallurgy and ceramic parts are predicted in close agreement to experimental findings.

Sintering theory developed continuously but slowly from the late 1940s. The most successful approaches to understand the mechanisms of neck growth and shrinkage have been the two-sphere model due to Frenkel[1] and Kuczynski[2] for the early sintering stages (particle bonding), the cylindrical pore channel model due to Coble[3] and the extrapolated two-particle model due to Kingery and Berg[4] for the intermediate shrinkage state, and the spherical pore model due to MacKenzie and Shuttleworth[5] for the late sintering stages. In the seventies, more sophisticated models (based on less simplified pore geometries and taking superposition of the various sintering mechanisms into account) were developed, for example, by Johnson,[6] Skorokhod,[7] Ashby,[8] Beere,[9] Scherer,[10] among many others (for reviews see, for example, Exner et al.,[11–14] Schatt,[15] German[16] or Olevsky[17]).

A similar development took place in liquid phase theory, where the early model due to Kingery,[18] has been the starting point for most of later and still ongoing theoretical work in spite of its geometric oversimplifications and lacking qualitative agreement with experimental observations. Extensive reviews on sintering models for liquid phase sintering are available (see, e.g. German,[19] Schatt,[15] Savitskii[20] or Exner and Arzt[13]).

Later theoretical work on solid and liquid state sintering considered additional effects like non-isothermal sintering, gravity, particle orientation, anisotropic shrinkage,[21] or superposition of external loads. In addition, sintering theory was also applied to new production methods like microwave sintering[22] or sinter forming.[23,24]

* Corresponding author.
E-mail address: hermann.reidel@iwm.fhg.dea (H. Riedel).

0955-2219/03/$ - see front matter
doi:10.1016/S0955-2219(03)00222-X

In most cases, the results were shown to agree well with experimental data.

The introduction of numerical methods helped to deal with more realistic situations and enables investigations of relevant technical applications. For example, finite element simulations of sintering in combination with appropriate material laws allow quantitative predictions of sinter distortions and part properties. In consequence, computer simulation could be a faster alternative in optimizing entire industrial processes compared to the conventional method of trial and error. In the following, the work of some groups which have investigated real parts by numerical simulation techniques is shortly summarized. For the work on simpler geometries or numerical work on the microscopic scale see the reviews cited earlier.

Predicting sinter distortions with the aim to minimize them by appropriate process control is one of the main aspects in the application of sintering simulations. One reason for distortions are intended property variations in gradient materials, in co-fired ceramics or in layered electronic circuits which usually result in strong warpage, unless the geometrical features and the sintering characteristics are carefully balanced. For example, Maximenko and Van der Biest,[25] who investigated the developing warpage during sintering of a graded cemented carbide and optimized the heat treatment by simulation, or Olevsky and Tikare,[26] who predicted the porosity distribution in bi-layered structures. Olevsky[17] presented results for the final porosity distribution and shape of a part bonded on a rigid substrate. In addition, this author has numerically investigated the sinter-forging of cylinders and the isothermal sintering of parts with non-uniform initial densities. Shinagawa[27,28] presents a viscoplastic constitutive model and simulation results on the warpage of graded powder compacts.

Further reasons for distortions are friction on the support plate and gravity especially in large and thin-walled parts. Bouvard and coworkers[29,30] investigated the deformation of sintering with and without gravity for several parts made of FE-based and WC-Co powders and found good agreement with experimental data. The influence of gravity and friction on shrinkage and deformation during firing of tableware plates is studied by Kraft et al.[31] Ganesan et al.[32] predicted the developing distortion during liquid phase sintering due to the viscous flow. At last, Shinagawa[33] has also used his model[28] for the prediction of shape changes due to gravity.

Temperature gradients may also play a role in developing distortions, especially in connection with microwave heating, since many materials absorb electromagnetic energy more effectively at higher temperatures, which tends to enhance temperature gradients and hence warpage.[22] For large parts temperature gradients during heating have to be considered in sintering simulations to get realistic results as investigated by Plankensteiner et al.[34] for large Mo-cylinders or Kraft et al.[31] for plates. These authors have coupled the sintering simulation with a heat transfer analysis. Several numerical studies (see e.g. Refs. [35–41]) had been performed for hipping to investigate the final shape of the part. Sinter forging of a simple cylinder was investigated e.g. by Jagota et al.,[42] Chenot[36] or by Olevsky.[17] Mori[43] used a finite element code for simulating non-uniform shrinkage in sintering ceramic powder compacts. However, the used rigid-plastic material model is not very suitable for simulating situations when diffusion and viscous mechanisms are dominant as in the case of sintering.

The sintering simulations of whole parts are sometimes based on results from numerical investigations of preceding production steps like uniaxial die compaction, isostatic compaction, slip and tape casting, debindering or drying. For example, the inhomogeneous green density distributions obtained after die compaction of ceramic powders leads to differential shrinkage of different volume elements and is the main reason for the developing distortions during sintering in this production route (see e.g. Mori,[43] Sanliturk et al.,[44] Doege et al.,[45] Kraft et al.,[46,47] or Olevsky[17]). Doege et al.[45] used a creep-like approach and predicted the final shape of complex parts considering an inhomogeneous initial density distributions determined by a compaction simulation. Sanliturk et al.[44] developed a numerical model which is based on the conservation-of-mass principle and investigated shape changes during sintering.

The group of the present authors has applied the finite element method to predict the sinter distortions with the aim to minimize them by appropriate process control. Several applications and materials have been studied.[31,34,46–51] This paper describes a comprehensive constitutive model for solid state sintering, which summarizes various aspects published previously.[52–60] It also extends the model to external loads several times higher than the sintering stress, a case not considered previously. A similar sintering model is used by Kanters et al.[61] A corresponding liquid phase sintering model and its implementation was published in.[50,62] This model was extended by Markondeya Raj et al.[63] to elliptical particles investigating anisotropic shrinkage. The solid state model had already been implemented in the implicit FE Code ABAQUS©/Standard and applied to the sintering of molybdenum cylinders.[34,51] An implementation for the explicit FE code ABAQUS©/Exlicit was performed recently.[23,24] To demonstrate the possibilities of the model the simulation of sintering (and powder compaction) of a face seal made of SiC is presented.

2. Solid state sintering model

The model presented is based on concepts developed, for example, by Ashby[8,64] and Arzt,[65] as far as sintering mechanisms are concerned, and on work of Scherer,[66] Abouaf et al.,[35] Jagota and Dawson,[67] and McMeeking and Kuhn,[68] as far as mechanical aspects are concerned. It combines results on second and third stage sintering with models for grain growth in porous solids.

The second and third sintering stages are characterized by open and closed porosity, respectively. In both stages, the pore surfaces are equilibrium surfaces, i.e. surfaces with minimum energy or uniform mean curvature.[16,53] In the first stage, the surface of the pore space is not yet in equilibrium, since it is still influenced by the initial shape of the powder particles. Although appropriate models for neck growth in the first stage are available,[52] they are not embodied in the present model. Rather a purely phenomenological factor is used to describe particle rearrangement, which is another process in the first sintering stage. Since rearrangement and non-equilibrium neck growth have similar consequences for the constitutive response and since a detailed description of non-equilibrium neck growth would increase the conceptual complexity of the whole model, both processes are jointly described by one phenomenological factor. Grain boundary diffusion is assumed to be the dominant transport mechanism, but bulk diffusion through the grains is also taken into account as a parallel transport path. Surface diffusion acts like a process in series to grain boundary diffusion.

2.1. The general form of the constitutive equation

If the external loads on the part are not too high the rates of stress-directed diffusion depend linearly on stress, and the macroscopic strain rate tensor must be a linear function of the stress tensor:

$$\dot{\varepsilon}_{ij} = \frac{\sigma'_{ij}}{2G} + \delta_{ij}\frac{\sigma_m - \sigma_s + \Delta p}{3K} \tag{1}$$

where the prime denotes the deviator, σ_m is the mean (or hydrostatic) stress, Δp is a gas overpressure which may develop in closed pores, δ_{ij} is the Kronecker symbol, G and K are shear and bulk viscosity, respectively, and σ_s is the sintering stress, which arises from the surface tension forces of the pores.

The densification rate is given by the trace of the strain rate tensor:

$$\dot{\rho} = -\rho\dot{\varepsilon}_{kk} = \rho\frac{\sigma_s - \sigma_m - \Delta p}{K} \tag{2}$$

where ρ is the relative density.

The dependences of G, K and σ_s on temperature, density, grain size and possibly on other internal variables will be specified by the detailed model to follow. The densification rate during pressureless sintering ($\sigma_m = 0$) decreases with the fourth power of the grain size, since $\sigma_s \propto 1/\text{grain size}$ and $K \propto (\text{grain size})^3$ (Ref. [65]).

2.2. The general form of the viscosities

The viscosities for a linear stress/strain-rate relation are written in the following form:

$$K_{lin} = \frac{kTR^3}{\Omega\delta D_b}((1-\theta)k_1 + \theta k_2)U;$$
$$G_{lin} = \frac{kTR^3}{\Omega\delta D_b}((1-\theta)g_1 + \theta g_2)U \tag{3}$$

where k is the Boltzmann constant, T the absolute temperature, Ω the atomic (or molecular) volume, R the grain radius, δD_b the grain boundary diffusion coefficient times grain boundary thickness; δD_b exhibits the usual Arrhenius-type temperature dependence with activation energy Q_b and pre-exponential factor δD_{b0}. Further, k_1 and g_1 are normalized bulk and shear viscosities for open porosity, k_2 and g_2 are normalized viscosities for closed porosity, θ gives a smooth transition from open to closed porosity, and U is a factor to describe the effect of grain rearrangement. Expressions for the normalized viscosities, for θ and for U are given in Sections 2.3–2.6. In this form the model leads to a linear stress/strain-rate relation, i.e. K_{lin} and G_{lin} are independent of the stress. The underlying assumption is that grain-boundaries and pore surfaces act as perfect sources and sinks for the diffusing atoms or vacancies.

A non linear relation is obtained if grain boundaries do not act as perfect sources and sinks for vacancies, i.e., if diffusion becomes source controlled. Burton[69] and Cocks[70] discuss the source-controlled mechanism and obtain a quadratic dependence of the creeprate on stress and an inverse linear dependence on grain size. Cocks also gives an interpolation formula between the regimes of source control and diffusion control. In terms of the viscosities this means:[23,24]

$$K = K_{lin}\left(1 + \frac{\alpha}{\bar{\sigma}R^2}\right); \quad G = G_{lin}\left(1 + \frac{\alpha}{\bar{\sigma}R^2}\right) \tag{4}$$

with the linear viscosities, G_{lin} and K_{lin}, and a correction due to source-controlled diffusion. Here α is a free parameter determining the deviation from linearity and $\bar{\sigma}$ is an effective stress given by:

$$\bar{\sigma} = \tfrac{1}{2}\left|\sigma_m - \sigma_s + \Delta p\right| + \tfrac{1}{2}\sigma_e \tag{5}$$

where σ_e is the von Mises equivalent stress. The relative effect of the source-controlled diffusion is larger at

smaller grain sizes and lower stresses, while at greater stresses the linear stress dependence is recovered.

It should be noted that an alternative source on non linearities in the stress–strain rate relation is the interaction between grain boundary and source diffusion. As Chuang et al., [71,72] show, this can lead to σ^3 and $\sigma^{3/2}$ dependences of the cavity growth rate under high tensile stresses. Similar effects can be expected for sintering under compressive stresses, if they are several times greater than the sintering stress.

The viscosities and the sintering stress are calculated for the equilibrium pore surfaces given in Ref. 53. Fig. 1 shows examples of equilibrium surfaces for open porosity. Grain boundary diffusion in the approximately circular grain contact areas is the dominant densification mechanism. At a certain density, neighboring contact areas touch one another pinching off pore channels leading to isolated pores. The relative density at which this transition from open to closed porosity occurs is given by the following relation which approximates the numerical results of Ref. 53:

$$\rho_{\mathrm{cl}} = 1.05 - 0.115\psi \tag{6}$$

with the dihedral angle defined by

$$\cos\psi = \frac{\gamma_b}{2\gamma_s} \tag{7}$$

where γ_{b} and γ_{s} are the specific energies of the grain boundary and the surface, respectively. Fig. 2 shows two different configurations of closed porosity in the third sintering stage.

2.3. The contributions of grain boundary, bulk and surface diffusion to the bulk viscosity

As stated earlier, grain boundary diffusion is considered to be the primary transport mechanism for densification. Surface diffusion is needed to spread the material that flows out of a grain boundary over the pore surface. In principle, the assumption of equilibrium pore shapes implies that surface diffusion is infinitely fast. Finite surface diffusivities lead to non-equilibrium pore surfaces.

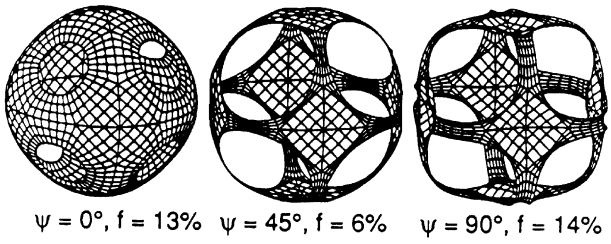

Fig. 1. Equilibrium grain surfaces for open porosity in the second sintering stage (ϕ = dihedral angle, f = porosity).

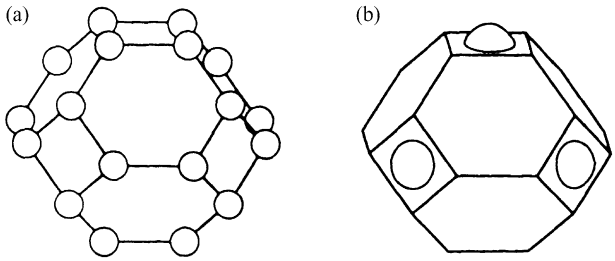

Fig. 2. Closed porosity located at grain corners (a) and in the spaces between next-nearest grain neighbors (b) in the third sintering stage.

However, the influence of finite, rather than infinite, surface diffusivities can be treated by an approximate method which is based on the assumption of equilibrium pore shapes.[54–57] One calculates the grain boundary and surface diffusion fluxes corresponding to a sequence of equilibrium configurations. Then one equals the dissipation rate associated with these fluxes to the negative rate of Gibbs free energy. In the resulting densification rates grain boundary and surface diffusion act like electric resistors in series. This approximation has been shown to give very accurate results compared to numerical solutions for pore shrinkage in a two-dimensional configuration,[57] and there is no reason to assume that it is not applicable to 3D configurations.

Bulk diffusion is generally understood as a parallel path to the grain boundary/surface diffusion path.[8,64] According to this understanding of the interaction between grain boundary, surface and bulk diffusion, the normalized bulk viscosities are written in the form:

$$k_i = \frac{(k_{ib} + k_{is})k_{iv}}{k_{ib} + k_{is} + k_{iv}} \tag{8}$$

The subscript i denotes open ($i=1$) and closed ($i=2$) porosity. The subscripts b, s and v denote grain boundary, surface and volume (or bulk) diffusion. The expressions for k_{ib} and k_{is} are taken from Refs. 54–56 and the contribution of volume diffusion is treated approximately as proposed by Ashby:[8,64]

$$k_{1\mathrm{b}} = \begin{cases} A_0 + A_1 f + A_2 f^2 & \text{for } \rho \geqslant 0.68 \\ A_9 \exp(-A_{10}(0.32 - f)) & \text{for } \rho < 0.68 \end{cases} \tag{9}$$

$$k_{1\mathrm{s}} = \frac{\delta D_{\mathrm{b}}}{\delta D_{\mathrm{s}}} k_{1\mathrm{b}} \frac{-2\ln\Phi - (3-\Phi)(1-\Phi)}{2(1-\Phi)^2} \tag{10}$$

$$k_{1\mathrm{v}} = \frac{\delta D_{\mathrm{b}}}{0.6RD_{\mathrm{v}}} k_{1\mathrm{b}} \tag{11}$$

with the relative density ρ, the porosity $f = 1-\rho$, the abbreviation $\Phi = 2(A_3 + A_4 f)^2$, the surface diffusion

coefficient, $\delta D_s = \delta D_{s0}\exp(-Q_s/R_gT)$ and the bulk diffusion coefficient $D_v = D_{v0}\exp(-Q_v/R_gT)$, where R_g is the gas constant; the functions of the dihedral angle, A_0 to A_{10}, are given in the Appendix. Further

$$k_{2b} = \frac{1}{18\rho}\left(-2\ln\omega_b - \frac{33}{64} + \omega_b - \frac{\omega_b^2}{16}\right) \tag{12}$$

$$k_{2s} = \frac{\delta D_b}{\delta D_s}\frac{1}{\rho}\left(A_5 + A_6\omega_b + A_7\omega_b^2\right) \tag{13}$$

where

$$\omega_b = A_8 f_b^{2/3} \tag{14}$$

is the area fraction of grain boundaries covered by pores, and

$$k_{2v} = \frac{\delta D_b}{0.6RD_v}\frac{1}{18\rho}\left(-2\ln\omega - \frac{33}{66} + \omega - \frac{\omega^2}{16}\right) \tag{15}$$

with $\omega = A_8 f^{2/3}$. The distinction between ω and ω_b is made since during grain growth, pores may detach from migrating grain boundaries (see Section 2.9). The volume fraction of pores that remain on grain boundaries, f_b, is given by

$$f_b = \begin{cases} f & \text{if } \rho < \rho_{cl} \text{ or } f > f_d \\ \beta_0 f - (\beta_0 - 1) f_d & \text{if } \rho > \rho_{cl} \text{ and } f_d > f > \dfrac{\beta_0 - 1}{\beta_0} f_d \\ 0 & \text{if } f < \dfrac{\beta_0 - 1}{\beta_0} f_d \end{cases} \tag{16}$$

Here β_0 describes the width of the range over which pore detachment occurs ($\beta_0 = 1.3$ is chosen here), and f_d is the porosity at which detachment occurs theoretically according to the condition derived in Refs. 58 and 59:

$$R^2 f_d \frac{1 - f_d^{1/3}}{1 - \omega_d} = 4.5\frac{\Omega\delta D_s}{kTM_b} \tag{17}$$

where $\omega_d = A_8 f_d{}^{2/3}$, and M_b is the grain boundary mobility (see Section 2.9). Kucherenko et al.[73] investigated the pore detachment by a more general numerical model considering also grain-boundary diffusion and the shrinkage of the pore as it migrates with the grain-boundary. Their results confirm the ones received in Ref. 58 for cases neglecting grain-boundary diffusion. If grain-boundary diffusion was considered the pore shrinkage due to this diffusion makes it somewhat less likely that a pore separates from a migrating grain-boundary.

2.4. The shear viscosity

For open porosity, shear viscosities were calculated in Refs. 54 and 68 to be:

$$g_1 = \beta_1 k_1 \tag{18}$$

An upper bound estimate for the ratio of shear to bulk viscosity is $\beta_1 = 0.6$[68] for freely sliding grain boundaries, while a self-consistent estimate is $\beta_1 = 0.27$[54]. In the present paper β_1 is considered as an adjustable parameter.

For closed porosity the following relation holds:[55]

$$g_2 = \beta_2\frac{(g_{2b} + g_{2s})g_{2v}}{g_{2b} + g_{2s} + g_{2v}} \tag{19}$$

with

$$g_{2b} = \frac{1}{\rho}\left(0.029 - 0.022\sqrt{\omega_b}\right) \tag{20}$$

$$g_{2s} = \frac{k_{2s}}{k_{2b}}g_{2b} \tag{21}$$

$$g_{2v} = \frac{1}{\rho}\left(0.029 - 0.022\sqrt{\omega}\right)\frac{\delta D_b}{0.6RD_v} \tag{22}$$

The dimensionless factor β_2 should be $\beta_2 = 1$ according to the self-consistent estimate given in Ref. 55, but it is considered as an adjustable parameter in this paper.

2.5. Interpolation between open and closed porosity

The transition parameter θ is assumed to vary from 0 to 1 in a density range from ρ_{lo} to ρ_{hi}

$$\theta = \begin{cases} 0 & \text{for } \rho \leqslant \rho_{lo} \\ 1 - \cos\left(\dfrac{\pi}{2}\dfrac{\rho - \rho_{lo}}{\rho_{hi} - \rho_{lo}}\right) & \text{for } \rho_{lo} < \rho < \rho_{hi} \\ 1 & \text{for } \rho \geqslant \rho_{hi} \end{cases} \tag{23}$$

$$\rho_{lo} = \rho_{cl} - 0.04; \quad \rho_{hi} = \rho_{cl} + 0.04 \tag{24}$$

with the relative density at pore closure ρ_{cl} from Eq. (6), and the arbitrarily chosen number 0.04 for the width of the transition range.

2.6. Particle rearrangement

The phenomenological term for grain rearrangement is written in the form

$$U = \begin{cases} \left(\dfrac{\rho - \rho_0 + 0.02}{0.63 - \rho_0 + 0.02}\right)^{\zeta} & \text{for } \rho < 0.63 \\ 1 & \text{for } \rho > 0.63 \end{cases} \tag{25}$$

where ρ_0 is the initial relative density, and the numbers 0.63 and 0.02 are chosen arbitrarily. The idea is that rearrangement can contribute to densification and

deformation only in the initial sintering stages. Above a certain density (here 63%, the relative density of a random dense sphere packing) rearrangement can make no further contribution to densification. If the parameter ζ is zero, the rearrangement term has no influence. In the following a relatively small, fixed value, $\zeta = 0.2$, is chosen, which means that the rearrangement term is considered to be not very important.

2.7. The sintering stress

Like the viscosities, the sintering stress is calculated by interpolating between the (numerical) results for open[53] and closed porosity[55] using the transition parameter θ:

$$\sigma_s = ((1-\theta)\sigma_{s1} + \theta\sigma_{s2})\frac{\gamma_s}{R} \tag{26}$$

with

$$\sigma_{s1} = \begin{cases} C_0 + C_1 f + C_2 f^2 & \text{for } \rho \geqslant 0.68 \\ C_5 \exp(-C_6(0.32 - f)) & \text{for } \rho < 0.68 \end{cases} \tag{27}$$

$$\sigma_{s2} = 2\left(C_3\frac{\rho}{f}\right)^{1/3} + \frac{2\sqrt{3}+1}{2}\left(\frac{3\rho}{\pi}\right)^{1/3}\cos\psi \tag{28}$$

The functions of the dihedral angle, C_0–C_6, are given in the Appendix.

2.8. Gas pressure

After pore closure entrapped gas can no longer escape from the pore space. If the gas cannot diffuse through the solid and if ideal gas behavior is assumed, the overpressure in the pore is

$$\Delta p = p_{ex,cl}\frac{1-\rho_{cl}}{1-\rho}\frac{\rho}{\rho_{cl}}\frac{T}{T_{cl}} - p_{ex} \tag{29}$$

where the subscript cl denotes the values of density, temperature and external pressure, p_{ex}, at the time of pore closure. In many cases the effect of gas pressure on the densification rate is negligibly small. In the calculations on SiC performed later, the sintering stress is found to be of the order of 3.5 MPa, whereas the gas overpressure is less than 0.3 MPa at relative densities up to 98%.

2.9. Grain coarsening

Sintering is usually accompanied by grain coarsening. The grain growth rate is described by the classical Hillert law[74] with two modifications:

$$\dot{R} = \frac{\gamma_b M_b}{4R}\frac{F_d}{F_p} \tag{30}$$

The grain boundary mobility exhibits an Arrhenius-type temperature dependence $M_b = M_{b0}\exp(-Q_b/R_gT)$. The first modification of Hillert's law is expressed by the factor F_d. It is introduced to account for the fact that the powder usually does not have the steady-state grain size distribution, which is implicit in the Hillert solution. The following form is chosen for F_d:

$$F_d = \frac{1}{1-\delta R_0/R} \tag{31}$$

where R_0 is the initial average grain radius and δ can lie between $-\infty$ and 1. In this paper $\delta = 0$ is assumed for the sintering simulations on SiC, which corresponds to Hillert's law without a correction for the size distribution. The second modification, expressed by the factor F_p in Eq. (30), arises from the drag that pores exert on migrating grain boundaries. The specific form of F_p is taken from Refs. 58,59 For open porosity ($\rho < \rho_{cl}$):

$$F_p = 1 - D_3\sqrt{f} + D_2R^2f^{3/2}\frac{kTM_b}{\Omega\delta D_s} \tag{32}$$

For closed porosity ($\rho > \rho_{cl}$):

$$F_p = 1 - \omega_b + D_1R^2f_b^{4/3}\frac{kTM_b}{\Omega\delta D_s} \tag{33}$$

The Ds are functions of the dihedral angle (see Appendix). The term $1-D_3f^{1/2}$ in Eq. (32) represents the area fraction of grain boundary relative to the total grain surface area. Since the pore drag model was not designed to be accurate for large porosities, this term may erroneously become negative. If this happens, $1-D_3f^{1/2}$ is set to a small positive value.

2.10. Summary of the model

Eqs. (1)–(33) define the solid state sintering model. Eqs. (1) and (30) are the most important ones, since they are the evolution equations for the strain rate and for the grain size. The other equations explain the quantities that appear in the evolution equations.

A PC-FORTRAN program for the solution of the equations for prescribed stresses was written and is used to adjust the model parameters for various materials. Adjusting the parameters by automatic methods is difficult due to the number of free parameters.

The whole set of equations has also been implemented in the implicit FE Code ABAQUS®/Standard as a user supplied material routine (UMAT) to simulate sintering of complex shaped parts like the one presented later. By using the coupled thermo-mechanical solver in ABAQUS the effect of inhomogeneous temperature distributions on the sinter distortion can be studied as well. An application to the sintering of Mo cylinders is described in Refs. 34 and 51. An explicit version of the UMAT was implemented in ABAQUS®/Explicit to simulate sinter forming processes.[23,24]

3. Material parameters of SiC for the solid state sintering model

In the simulations presented later an α-silicon–carbide powder of Wacker Ceramics Kempten, Ekasic® D, was used. This powder contains C, B and Al als sintering aids in concentrations below 1%. To determine the material parameters of the model, so-called sinter forging or load dilatometry tests had been carried out.

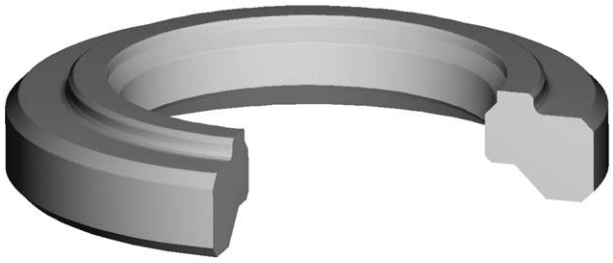

Fig. 3. Face seal.

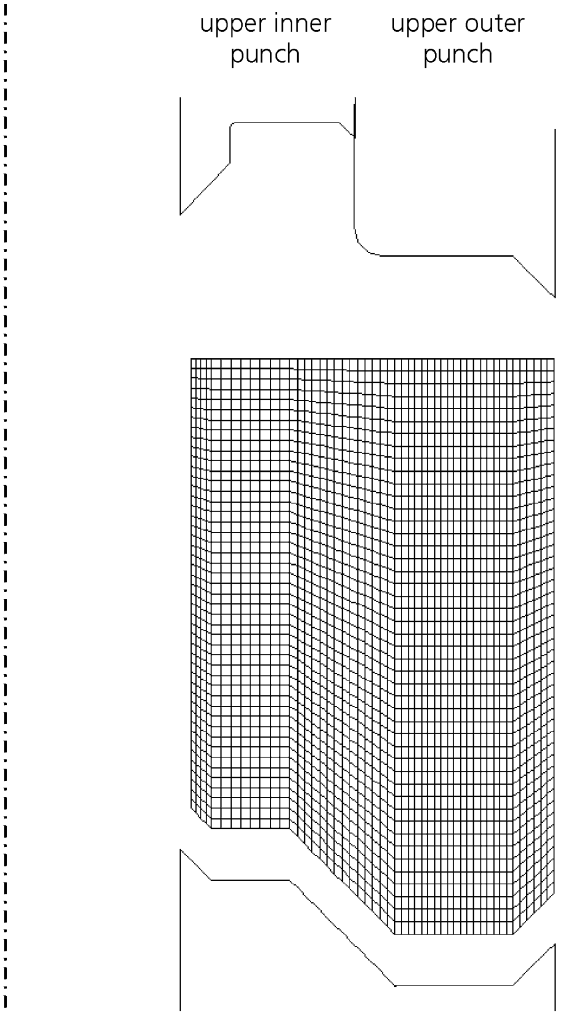

Fig. 4. Finite element of the mesh of the powder and the punches before compaction (the inner and outer die are not shown and the punch positions are shifted away from the powder).

Several small cylindrical specimens were subjected to different axial loads during sintering, and the axial and radial strains were continuously measured. The parameter fit was done by using the PC-FORTRAN program and varying the parameters by hand, until the simulated behavior agrees with the measured one. For details of the measurement and a description of how the parameters were determined as well as comparisons of experiment and model predictions see Riedel and Blug.[60]

At this point only the parameters determined are summarized for free sintering conditions (without a substantial external load): initial grain radius $R_0 = 2.4\times10^{-7}$ m, external gas pressure $p_{ex} = 1.0\times10^5$ Pa, atomic volume $\Omega = 2.07\times10^{-29}$ m^3, grain boundary diffusion $\delta D_{b0} = 2.3\times10^{-9}$ m^3/s, $Q_b = 600$ kJ/mol, surface diffusion $\delta D_{s0} = 4.0\times10^{-2}$ m^3/s, $Q_s = 600$ kJ/mol (not fitted, but set to a high value), volume diffusion $D_{v0} = 1.2\times10^{15}$ m^2/s, $Q_v = 1300$ kJ/mol, grain boundary mobility $\gamma_b M_{b0}/4 = 3.8\times10^5$ m^2/s, $Q_m = 900$ kJ/mol, surface energy $\gamma_s = 1.0$ J/m^2, dihedral angle

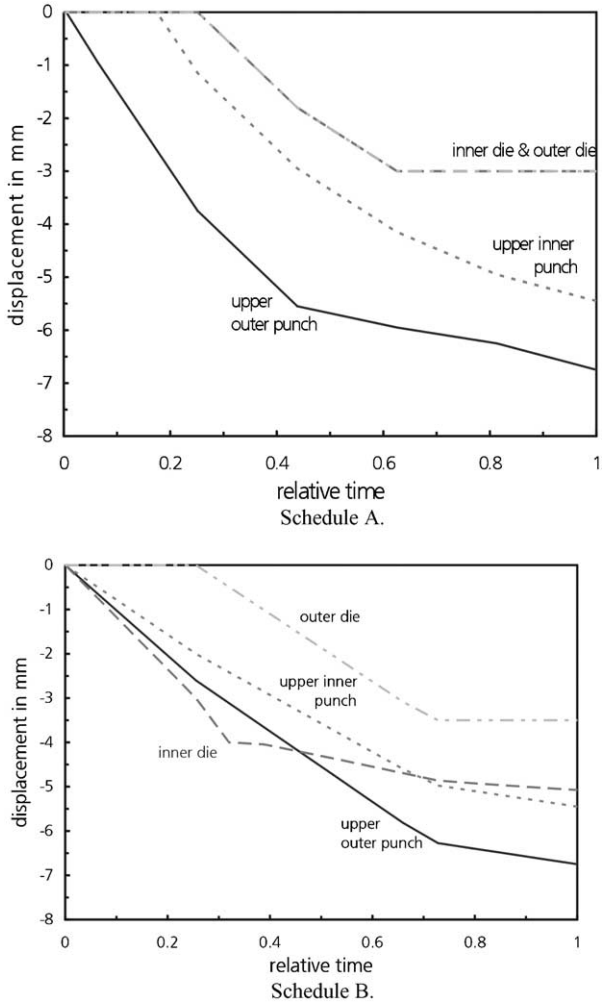

Fig. 5. Pressing schedules (the displacements are related to the fixed lower punch).

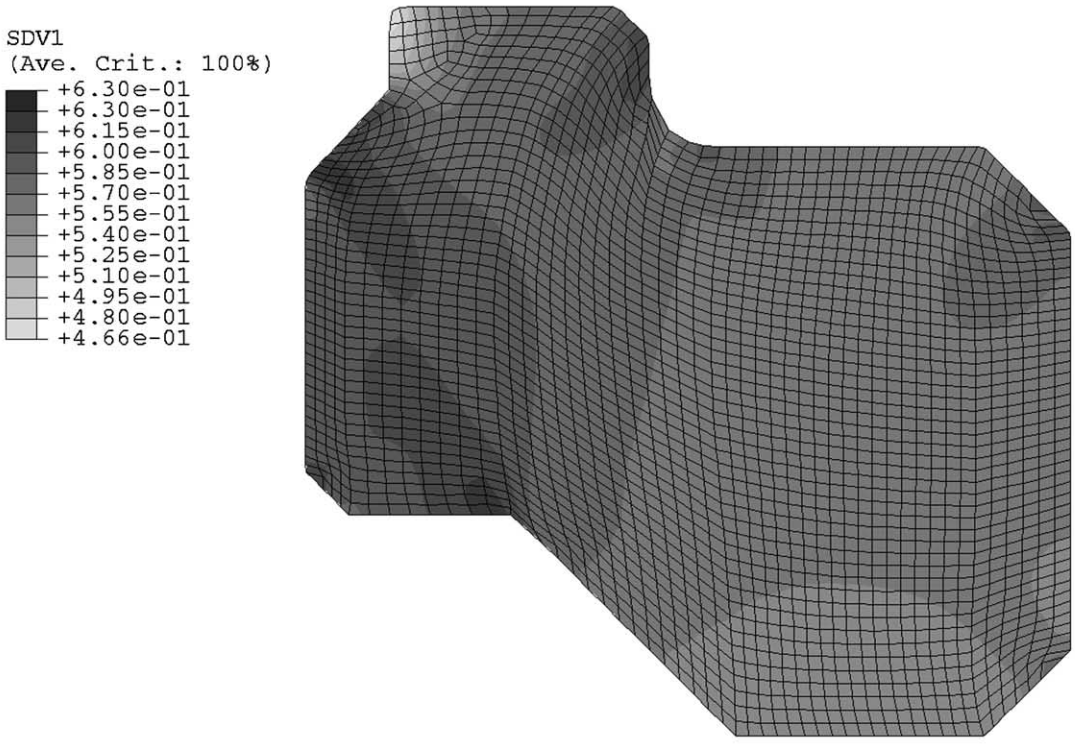

Schedule A.

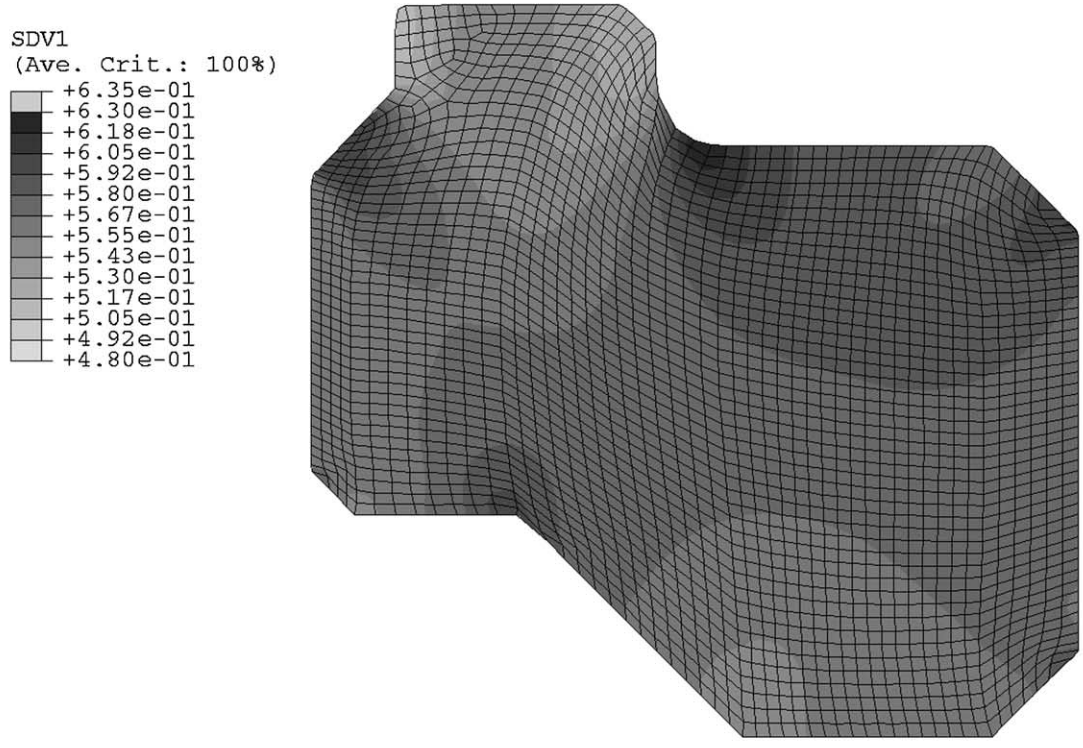

Schedule B.

Fig. 6. Density distribution after removal of the binder (SDV1 = relative density related to theoretical full density of 3.19 g/cm^3).

$\psi = 70°$, exponent in rearrangement term $\zeta = 0.2$, initial grain size distribution $\delta = 0$, pore detachment $\beta_0 = 1.3$, G/K for open porosity $\beta_1 = 1.08$, multiplier for closed porosity $\beta_2 = 4$, source controlled diffusion $\alpha = 0$, theoretical density of fully dense material $\rho_{th} = 3.19$ g/cm^3.

The adjustment of the model to the experiments had unequivocally required an unusually high activation energy for bulk diffusion. The difference is tentatively explained in Ref. 60 by the effect of the sintering aids on the diffusion mechanisms. A new adjustment of the parameters considering source-controlled diffusion would probably decrease the value as was observed in the fitting procedure of the parameters for modeling sinter forming[24] but was not performed yet. Nevertheless, the model predictions with the fitted parameters agree quite well with the measurements.[60]

4. Simulation of a face seal

To demonstrate the possibilities of the model presented earlier the production process of a face seal made of SiC is investigated. Fig. 3 shows the geometry, which is axisymmetric. This face seal is made by powder die compaction followed by the sintering process. Since the green density distribution obtained in the compaction calculation serves as the starting condition for the sintering simulation (initial relative density ρ_0 in the model) this step must be simulated also. For details on compaction simulations see e.g. Refs. 47 and 75

The material parameters for the compaction simulation had been also measured. The densification behavior was investigated in an uniaxial compaction experiment and the parameters of the extended Drucker–Prager–Cap model[75] used in the calculation were adjusted accordingly. The friction coefficient between powder and hard metal tooling was measured to be 0.25. The fill density was determined to be 0.93 g/cm^3 corresponding to a relative density of 0.292.

In most compaction simulations the tools are modeled as rigid bodies. This is acceptable, because the deformation of the tools has only an insignificant influence on the density distribution in the green body. Fig. 4 shows the axisymmetric mesh of the face seal used together with the punches. The part is pressed with a multi-level tool. The upper punch is divided. The two upper punches, the lower punch and the two dies can be controlled independently. The pressing schedule, which until now is mainly obtained by trial and error combined with a lot of experience, can have a significant influence on the formation of cracks as well as on the green density distribution. The latter is demonstrated by using two schedules. The second is comparable to an actual schedule used in the production of this face seal. The first one had been tried earlier. Fig. 5 shows the two pressing schedules. The displacements shown are related to the lower punch whose position is fixed in the simulation. Since the compaction calculation is time-inde-

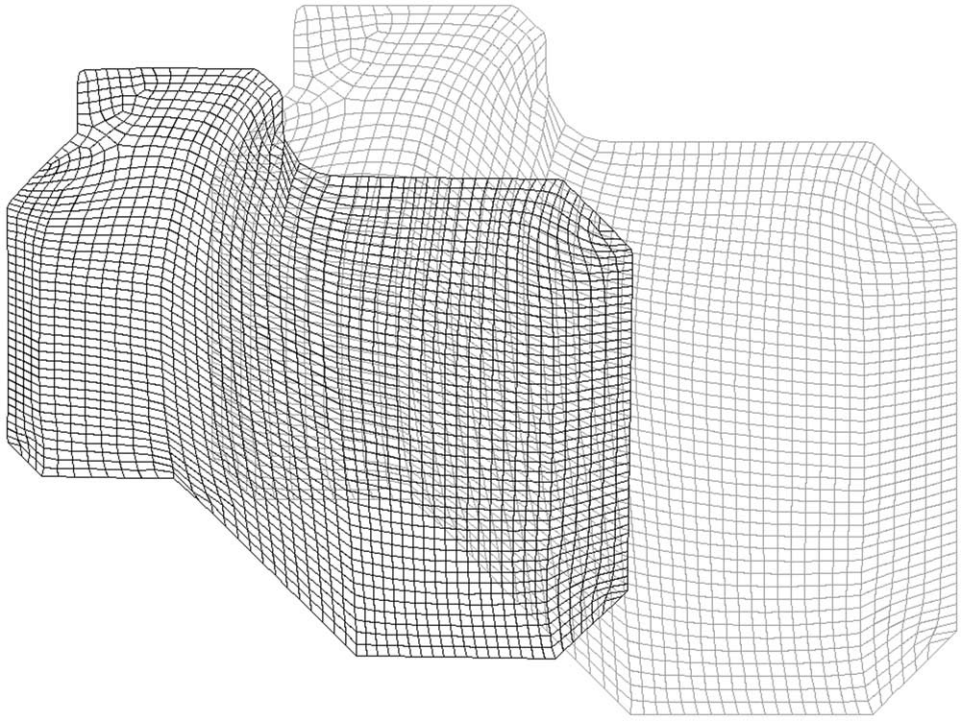

Fig. 7. Shape of the face seal before (gray) and after (black) sintering for schedule B.

pendent, a relative time corresponding to the complete compaction time is given.

Fig. 6 shows the resulting density distributions of the green body after removal of the binder for the two compaction schedules. It could be clearly seen that the distributions are inhomogeneous and different from each other. It should be mentioned that the initial filling heights and punch positions had been identical. The relative densities for both are in the range from 0.48 to 0.63. These distributions serve as starting conditions for the sintering simulations indicating already that some warpage will occur. However, without simulation the final shape could not easily be foreseen. For the sintering simulation a new mesh is often necessary due to the fact that the pressing mesh is more or less distorted especially if the powder flows around corners. In the present study, the resulting mesh after compaction was partly remeshed by hand because the area below the intruding upper inner punch was too heavily distorted. To transfer the results (density distribution) from the compaction simulation to the sintering simulation a specially developed transfer program was used. It interpolates the predicted green densities at the nodes of the press mesh to the new nodes of the sinter mesh using the shape functions. Computation times are in the order of 2 h for both the pressing and the sintering simulation using a LINUX PC-workstation with 1.6 GHz.

For the sintering simulation a heating rate of 20 K/min was assumed. The sintering temperature was 2200 °C with a hold time of 50 min at 1 bar gas pressure. The other material parameters of the model are given in the previous section. Fig. 7 shows the calculated shape of the face seal before and after sintering for schedule B. The shrinkage of about 16% is evident. The distortion could not so clearly be seen. Therefore, the distorted shape predicted after sintering for both schedules is magnified in Fig. 8. While both green bodies show density variations in same order (see Fig. 6) the distortion after sintering of the part pressed with schedule B is smaller indicating that the different shrinkage rates are partly compensated in this case. For schedule A, the lower density in the right leads to a higher shrinkage and, as a result, tilting of the cross section of the ring.

Several further variations of the pressing schedule were investigated but a perfect schedule which does not lead to any distortion could not be found for this part and it is likely that none exists for a shape like this if the tooling is not divided into even more independently controllable punches. This, however, would increase the production cost beyond an acceptable limit. If further reductions of the warpage are desired, the punch surfaces should be shaped as to compensate the remaining distortion. The proper shape of the punches can be found by simulation in a few iterative steps as demonstrated for different parts in Refs. 76–78.

The final density distribution (or porosity as this is one minus relative density) is shown in Fig. 9. For the sintering conditions used full density is not reached. Again the final porosity distribution is different for the two schedules. Depending on the local initial density, the final density varies spatially for about 3 abs.%. The predicted distribution of the final grain size is almost homogeneous (Fig. 10). The initial grain radius was 0.24 μm. The sintering model predicts two other results: Fig. 11 shows the final gas pressure in the closed pores with the maximum up to 0.8 MPa at sintering temperature. However, at room temperature the pressure will be smaller. Fig. 12 shows the temperature at which pore closure occurs. The latter lies in relatively small temperature range.

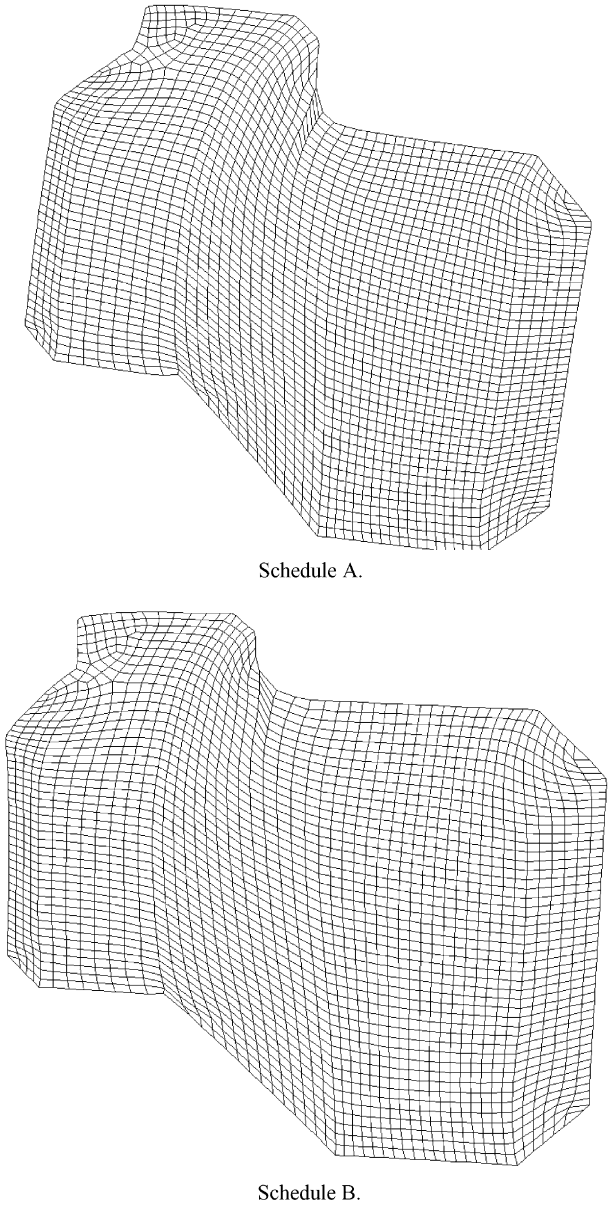

Fig. 8. Predicted shape after sintering (magnified).

To investigate the sintering behavior in more detail, an element with the average relative density of the whole face seal, which is calculated to be 0.57, is selected. Fig. 13 shows the development of the relative density as a function of the processing time and corresponding temperature. Sintering starts after about 20 min and a temperature of approximately 1800 °C. The final relative density reached is 0.977 and did not increase further after about 60 min. If the pressure in the furnace would be lowered to 0.1 bar the density would increase 0.983. The sintering stress is shown in Fig. 14. The maximum sintering stress occurs shortly

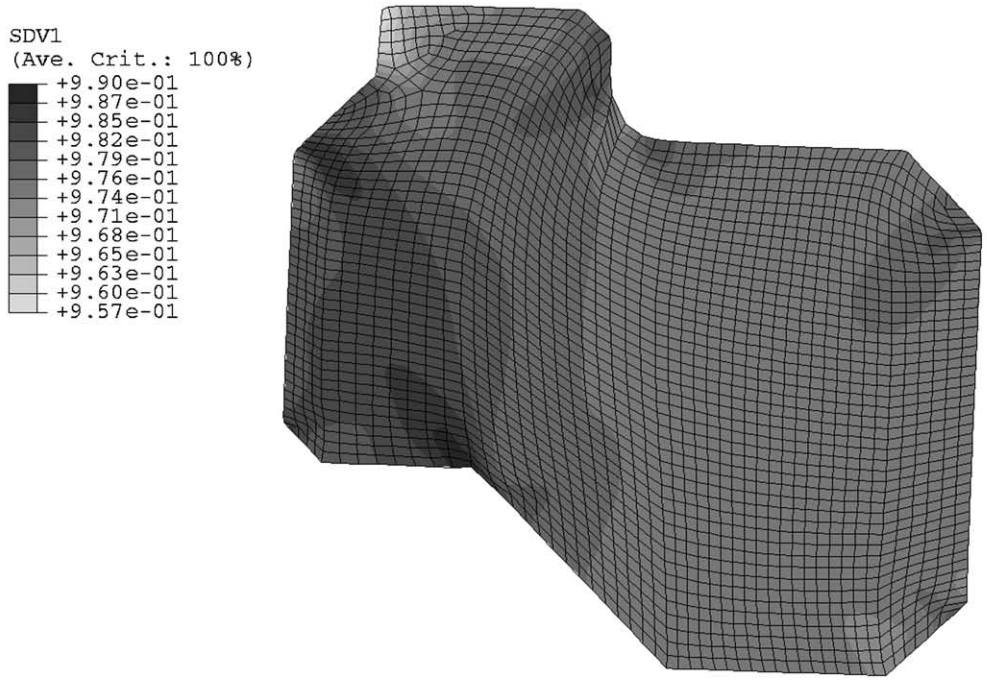

Schedule A.

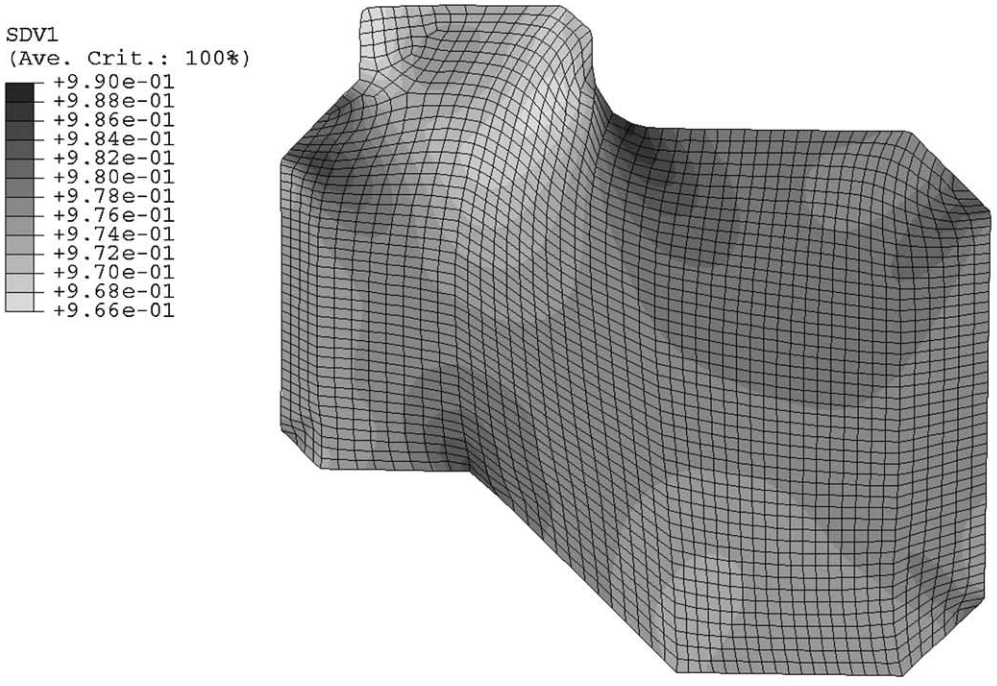

Schedule B.

Fig. 9. Final density distribution (SDV1 = relative density related to theoretical full density.

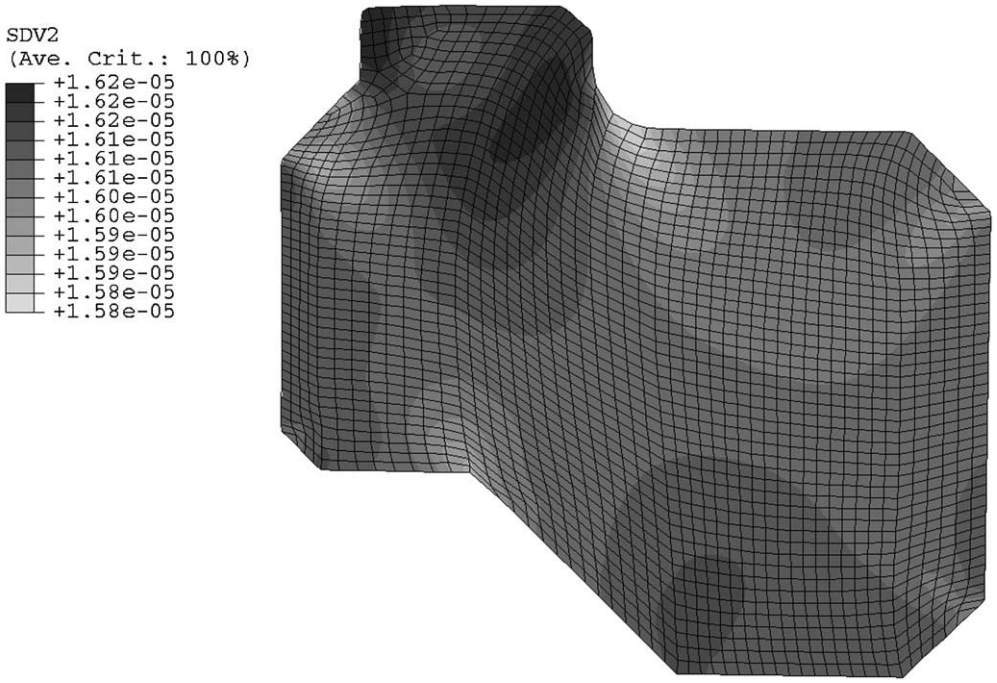

Fig. 10. Final grain size distribution (SDV2 = grain radius in m).

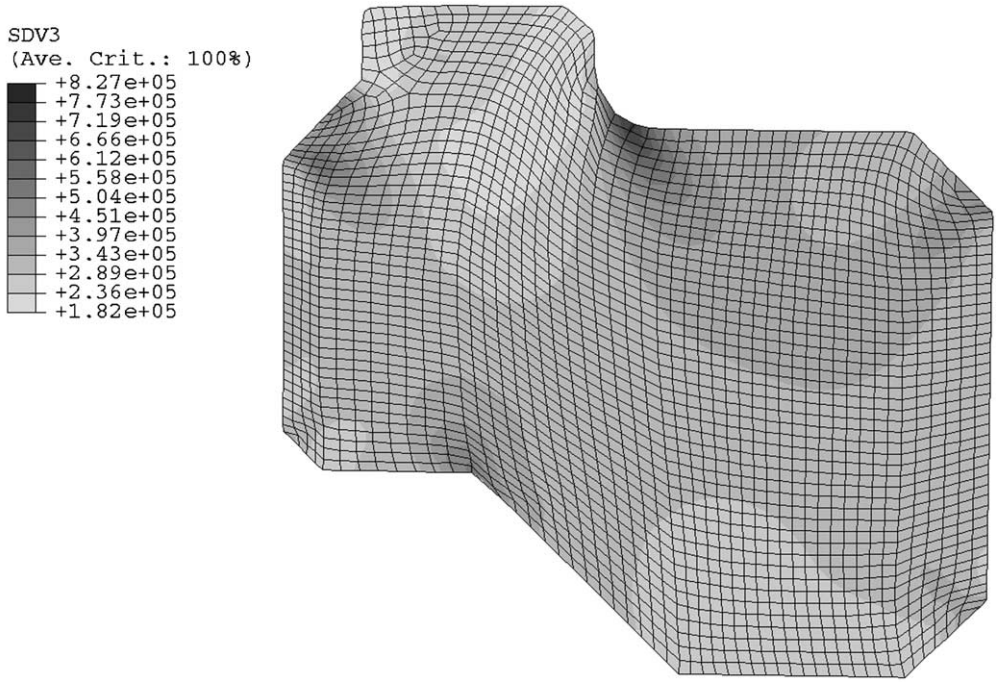

Fig. 11. Gas pressure in a closed pore after sintering (still at sintering temperature) (SDV3 = pressure in Pa).

before the maximum temperature is reached and decreases significantly afterwards. The development of the pressure in a closed pore is plotted in Fig. 15. Under the used sintering conditions the temperature when pore closure occurs is 2063 °C. At this point an increase in the sintering stresses starts. Fig. 16 shows the increase in grain size. In contrast to the almost constant density the grain coarsens further during the high holding temperature. Lastly, in Fig. 17 the dependence of the final density and the sintering stress from the initial green density are shown in the range of green densities predicted in the compaction simulation.

Finally, the model predictions are compared with a simplified model developed and implemented as a user

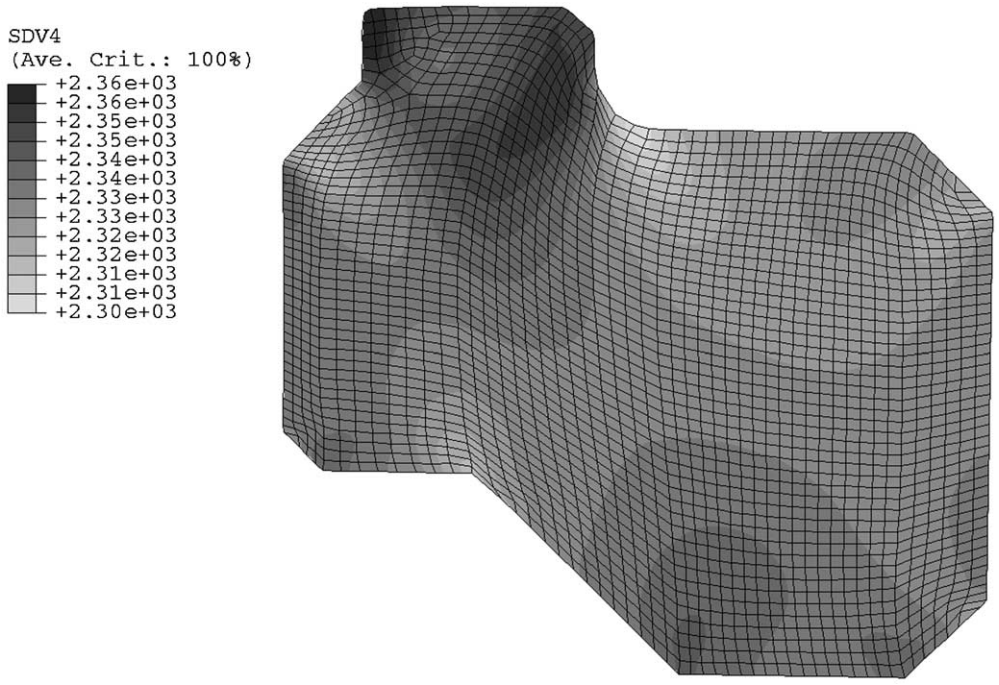

Fig. 12. Temperature when pore closure occurs (SDV4 = temperature in K).

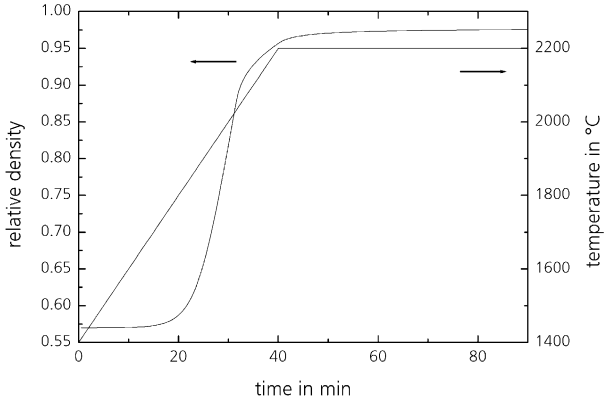

Fig. 13. Development of relative density for the average initial density of 0.54.

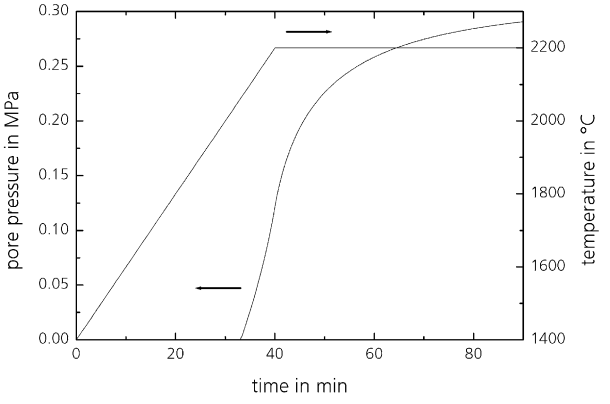

Fig. 15. Development of pore pressure for the average initial density.

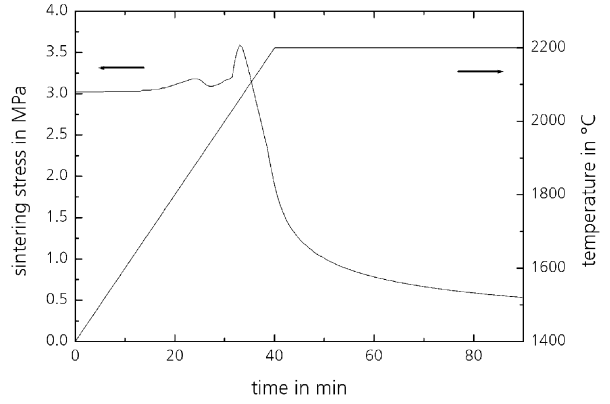

Fig. 14. Development of sintering stress for the average initial density.

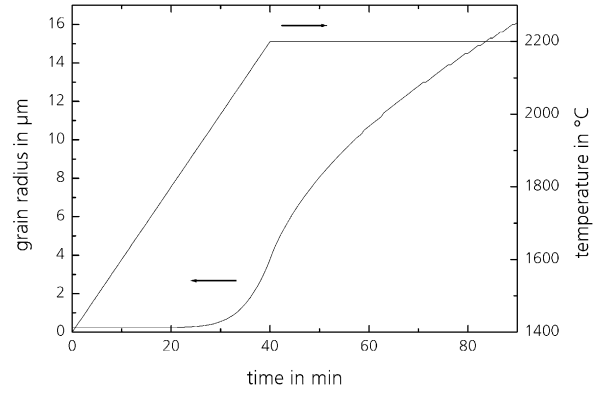

Fig. 16. Development of grain radius for the average density of 0.57.

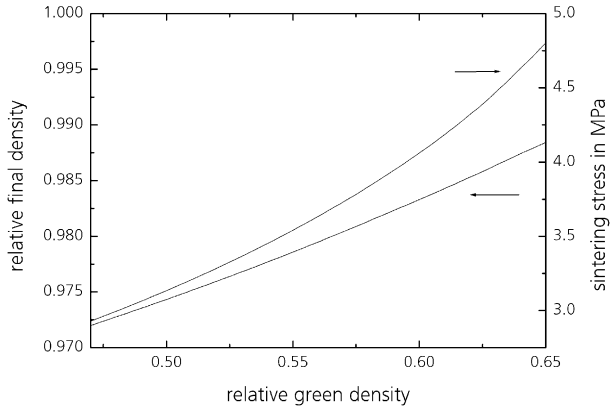

Fig. 17. Final density and sintering stress different initial densities.

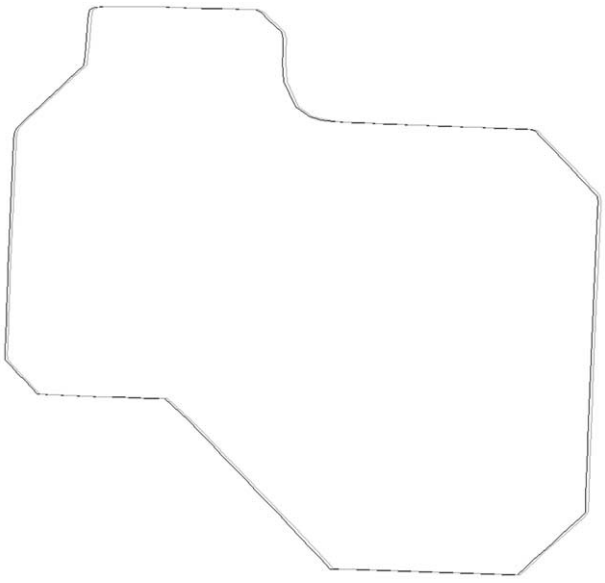

Fig. 18. Predicted contour after sintering for the complete model (black) and the simplified one (gray) for pressing schedule A.

subroutine in ABAQUS®/Standard by Riedel et al.[48,49,79] In this model, grain boundary diffusion is considered as the only transport mechanism and a simple two-dimensional hexagonal grain structure is considered with pores at the triple points. Grain growth is not considered. Fig. 18 shows the predicted contour after sintering for the complete model and for the simplified one. The comparison is shown for pressing schedule A since for this schedule the distortion is larger. Both sintered shapes are nearly identical. However, since the simplified model predicts full density for the sintering conditions given, the simplified model should be used only in cases where nearly full density is expected.

5. Conclusions

A comprehensive model of solid state sintering was presented which combines previous models on various stages of sintering and grain coarsening. This model consists of a set of equations which is cast in a FORTRAN program for the analysis of sinter and sinter forging tests. It is also implemented as a user defined material routine UMAT for the finite element code ABAQUS® both in an implicit and an explicit version. It is possible to adjust the model parameters such that the model describes the densification, the deformation and the grain growth kinetics accurately. In this sense the model, especially in conjunction with the finite element method, is well suited to describe technological sintering processes. In summary, by computational optimization of the individual production steps suggestions can be made to improve the final properties of the produced part.

The sintering simulations presented for a face seal made of SiC demonstrate that the initial density distribution significantly affects the final warpage after sintering. Thus, determining this initial distribution, for example, by simulating the compaction process should be made most precisely. For the sintering simulation itself, some porosity remains and is spatially distributed in a non-uniform manner with a contour similarly to the corresponding green density distribution. Depending on the local initial density, the final density varies spatially for about 3 abs.%. The final grain size is nearly homogeneous. The sintering stress reaches 4.5 MPa in maximum while the final overall pore pressure at sintering temperature is up to 0.8 MPa.

Finally, the shape predictions of the model are compared with a simplified solid state sintering model and it is found that for cases where full density is expected the predicted distortions are nearly identical. However, the simplified model did not account for some effects (e.g. grain growth) and should be used only in cases where nearly full density is expected.

Acknowledgements

The authors are sincerely grateful to Mr. Blug for performing the experiments and want to thank Wacker Ceramics for the good co-operation. Part of the work was financially supported by the German Ministry of Research (BMBF) through grant number 03N8009A.

Appendix. Functions of the dihedral angle used in the model

In the following equations ψ is measured in radian:

$$A_0 = 0.014573 + 0.0063822\psi + 0.0009983\psi^2$$
$$A_1 = -0.092348 - 0.028098\ \psi + 0.016495\ \psi^2$$
$$A_2 = 0.16242 - 0.0062352\ \psi - 0.022826\ \psi^2$$
$$A_3 = 0.5998 + 0.00533\ \psi$$
$$A_4 = -1.271 + 0.4144\ \psi$$

$$A_5 = \frac{-48\ln\left(\cos\frac{\psi}{2}\right) - 12 + 6\cos\psi + 14\cos^2\psi - 9\cos^3\psi + \cos^5\psi}{9(2+\cos\psi)^2(1-\cos\psi)^4}$$

$$A_6 = \frac{3+\cos\psi}{18(2+\cos\psi)(1+\cos\psi)}$$

$$A_7 = \frac{2+\cos\psi}{144(1+\cos\psi)^2}$$

$$A_8 = \frac{3\sin^2\psi}{2C_3^{2/3}}$$

$$A_9 = A_0 + 0.32\ A_1 + 0.1024\ A_2$$
$$A_{10} = (A_1 + 0.64\ A_2)/A_9$$

$$C_0 = -4.069 + 6.557\ \psi + 0.0253\ \psi^2$$
$$C_1 = 26.75 - 42.58\ \psi + 5.986\ \psi^2$$
$$C_2 = -51.01 + 82.12\ \psi - 18.56\ \psi^2$$
$$C_3 = 3/2\ (2 - 3\ cos\ \psi + cos^3\ \psi)$$
$$C_4 = 3(\psi - \pi/6) - 2\sqrt{3}\ cos\ \psi\ sin\ (\psi - \pi/6)$$
$$C_5 = C_0 + 0.32\ C_1 + 0.1024\ C_2$$
$$C_6 = (C_1 + 0.64\ C_2)/C_5$$

$$D_1 = \frac{1}{3C_3^{1/3}}$$

$$D_2 = 0.7\frac{2C_4 + (\psi - \pi/6)\left(4\cos^2\psi - 3\right)}{C_4^{3/2}}$$

$$D_3 = 2\sqrt{2}\frac{\sin(\psi - \pi/6)}{C_4^{1/2}}$$

References

1. Frenkel, J., Viscous flow of crystalline bodies under the action of surface tension. *J. Phys. USSR*, 1945, **9**, 385–391.
2. Kuczynski, G. C., Self diffusion in sintering of metallic particles. *Met. Trans.*, 1949, **185**, 169–178.
3. Coble, R. L., Sintering of crystalline solids. I. Intermediate and final state diffusion models. *J. Appl. Phys.*, 1961, **32**, 787–792.
4. Kingery, W. D. and Berg, M., Study of the initial stages of sintering of solids by viscous flow, evaporation-condensation and self-diffusion. *J. Appl. Phys.*, 1955, **26**, 1205–1212.
5. Mackenzie, J. K. and Shuttleworth, R., A phenomenological theory of sintering. *Proc. Phys. Soc. B*, 1949, **62**, 833–852.
6. Johnson, D. L., New method for obtaining volume, grain-boundary, and surface diffusion coefficients from sintering data. *J. Appl. Phys.*, 1969, **40**, 192–200.
7. Skorokhod, V. W. and Solonin, S. M., *Sov. Powder Metall. Met. Ceram.* 1972, 141.
8. Ashby, M. F., A first report on sintering diagrams. *Acta Metall.*, 1974, **22**, 275–289.
9. Beere, W., The second stage sintering kinetics of powder compacts. *Acta Metall.*, 1975, **23**, 139–145.
10. Scherer, G. W., Sintering of low-density glasses. *J. Am. Ceram. Soc.*, 1977, **60**, 236.
11. Exner, H. E., Principles of single phase sintering, In *Reviews on Powder Metallurgy and Physical Ceramics*, Vol. 1,. Freund Publishing House, Tel Aviv, 1979.
12. Exner, H. E., Solid-state sintering: critical assessment of theoretical concepts and experimental methods. *Powder Metall. Int.*, 1980, **4**, 203–209.
13. Exner, H. E. and Arzt, E., Sintering processes. In *Physical Metallurgy, 4th edn. Vol. 3*, ed. R. W. Cahn and P. Haasen. Elsevier Science, Amsterdam, 1996, pp. 2628–2662.
14. Exner, H. E. and Kraft, T., Review on computer simulations of sintering processes, In: *Powder Metallurgy World Congress 1998*, Vol. 2. EPMA, Shrewsbury, UK, 1998, pp. 278–283.
15. Schatt, W., *Sintervorgänge*. VDI-Verlag, Düsseldorf, 1992.
16. German, R. M., *Sintering Theory and Practice*. John Wiley & Sons, New York, 1996.
17. Olevsky, E. A., Theory of sintering: from discrete to continuum. *Mater. Sci. Eng. R*, 1998, **23**, 41–100.
18. Kingery, W. D., Densification during sintering in the presence of a liquid phase. I. Theory. *J. Appl. Phys.*, 1959, **30**, 301–306.
19. German, R. M., *Liquid Phase Sintering*. Plenum Press, New York, 1985.
20. Savitskii, A. P., *Liquid Phase Sintering of Systems with Interacting Components*. Russian Academy of Sciences, Tomsk, 1993.
21. Markondeya Raj, P., Odulena, A. and Cannon, W. R., Anisotropic shrinkage during sintering of particle-oriented systems numerical simulation and experimental studies. *Acta Mater.*, 2002, **50**, 2559–2570.
22. Riedel, H. and Svoboda, J., Simulation of microwave sintering with advanced sintering models. In *Proceedings of the 8th Ampere Conference, Bayreuth, 2001*, (in press).
23. Reiterer, M., Kraft, T., Kauermann, R. and Riedel, H., Modelling of the sinter forging process of reaction bonded alumina, in: *Materials Week 2001*. Werkoffwoche-Partnerschaft GbR, Frankfurt. Available: http://www.materialsweek.org (only on CD).
24. Reiterer, M., Kraft, T. and Riedel, H., Manufacturing of a gear wheel made from reaction bonded alumina—numerical simulation of the sinterforming process. *J. Eur. Ceram. Soc.* (in press).
25. Maximenko, A. and Van der Biest, O., Modeling of sintering WC-Co functionally graded materials. In *Recent Developments in Computer Modelling of Powder Metallurgy Processes, NATO Advanced Research Workshop, Series III: Computer and Systems Science—Vol. 176*, ed. A. Zavaliangos and A. Laptev. IOS Press, Amsterdam, 2001, pp. 105–111.
26. Olevsky, E. A. and Tikare, V., Combined macro-meso scale modeling of sintering: part i: continuum approach. In *Recent Developments in Computer Modelling of Powder Metallurgy Processes, NATO Advanced Research Workshop, Series III: Computer and Systems Science—Vol. 176*, ed. A. Zavaliangos and A. Laptev. IOS Press, Amsterdam, 2001, pp. 85–93.
27. Shinagawa, K., Deformation analysis of graded powder compacts during sintering. In *Functionally Graded Materials 1996*, ed. I. Shiota and M. Y. Miyamoto. Elsevier Science Publishers, Amsterdam, 1997, pp. 69–74.
28. Shinagawa, K., Finite element simulation of powder compacts and constitutive equation for sintering. *JSME Int. J. Series A*, 1996, **39**, 565–572.
29. Gillia, O. and Bouvard, D., Continuum modelling of sintering of powder compacts. In *Recent Developments in Computer Modelling of Powder Metallurgy Processes, NATO Advanced Research Workshop, Series III: Computer and Systems Science—Vol. 176*, ed. A. Zavaliangos and A. Laptev. IOS Press, Amsterdam, 2001, pp. 122–134.
30. Lame O. and Bouvard, D., Viscosity measurements during sintering of iron-based powder compacts, In: *European Congress on*

Powder Metallugy 2001, Vol. 3. EPMA, Shrewsbury, 2001, pp. 222–227.
31. Kraft, T., Riedel, H., Raether, F. and Becker, F., Simulation des Brennprozesses bei der Herstellung von Gebrauchskeramiken. *Keramische Zeitschrift*, 2002, **54**, 374–381.
32. Ganesan, R., Griffo, A. and German, R. M., Finite element modeling of distortion during liquid phase sintering. *Metall. Mater. Trans. A*, 1998, **28**, 659–665.
33. Shinagawa, K., Finite element analysis of microscopic material behavior in sintering and prediction of macroscopic shape change in sintered bodies, In *Proceedings of 3rd Asia-Pacific Symposium AEPA,*. 1996, pp. 439–444.
34. Plankensteiner, A. F., Parteder, E., Riedel, H. and Sun, D. -Z., Micromechanism based finite element analysis of the sintering behavior of refractory metal parts using ABAQUS. In *ABAQUS User World Congress, Chester*. 1999, pp. 643–657.
35. Abouaf, M., Chenot, J. L., Raisson, G. and Baudin, P., Finite element simulation of hot isostatic pressing of metal powders,. *Int. J. Numer. Methods Engng*, 1988, **25**, 191–212.
36. Chenot, J. L., Finite element simulation of powder forming. In *Numerical Methods in Industrial Forming Processes, Numiform 89*, ed. E. G. Thompson, R. D. Wood, O. C. Zienkiewicz and H. Samuelson. A.A. Balkema, Rotterdam, 1989, pp. v.
37. Nakagawa, T. and Nohara, A., Process simulations of HIP and CIP. In *Comp. Aided Innovation of New Materials*, ed. M. Doyam, T. Suzuki, J. Kihara and R. Yamamoto. North-Holland, Amsterdam, 1991, pp. 661–666.
38. Dellis, C., Bouaziz, O. and Moret, F., 3D modelling of hot isostatic pressing for stainless steel powder, In *Powder Metallurgy World Congress 1998*, Vol. 2, EPMA, Shrewsbury, UK, 1998, pp. 502–507.
39. Baccino, R. and Moret, F., Numerical modeling of powder metallurgy processes. *Mater. Design*, 2000, **21**, 359–364.
40. Wikman, B., Svoboda, A. and Häggblad, H., Å. *A combined material model for numerical simulation of hot isostatic pressing. Comp. Methods Appl. Mech. Eng*., 2000, **189**, 901–913.
41. Ouedraogo, F., Sanchez, L., Stutz, P. and Federzoni, L., Numerical prediction of the final shape of a test part formed by HIP, In *European Congress on Powder Metallugy 2001*, Vol. 3, EPMA, Shrewsbury, 2001, pp. 234–239.
42. Jagota, A., Mikeska, K. R. and Bordia, R. K., Isotropic constitutive model for sintering particle packings. *Am. Ceram. Soc*., 1990, **73**, 2266–2273.
43. Mori, K., Finite element simulation of nonuniform shrinkage in sintering of ceramic powder compact. In *Numerical Methods in Industrial Forming Processes, Numiform 92*, ed. J. L. Chenot, R. D. Wood and O. C. Zienkiewicz. A.A. Balkema, Rotterdam, 1992, pp. 69–78.
44. Sanliturk, K. Y., Aydin, I. and Briscoe, B. J., A finite-element approach for the shape prediction of ceramic compacts during sintering. *J. Am. Ceram. Soc*., 1999, **89**, 1748–1756.
45. Doege, E., Bagaviev, A. and Hanini, K., FEM Simulation der Prozessschritte Pulverpressen/Sintern. *Mat.-wiss. Werkstofftech*, 2001, **32**, 57–61.
46. Kraft, T., Riedel, H., Stingl, P. and Wittig, F., Finite element simulation of die pressing and sintering. *Adv. Engng. Mater*., 1999, **1**, 107–109.
47. Kraft, T. and Riedel, H., Numerical simulation of die compaction and sintering. *Powder Metall*, 2002, **45**, 227–231.
48. Riedel, H. and Sun, D.-Z., Simulation of die pressing and sintering of powder metals, hard metals and ceramics. In *Numerical Methods in Industrial Forming Processes, Numiform 92*, ed. J. L. Chenot, R. D. Wood and O. C. Zienkiewicz. A.A. Balkema, Rotterdam, 1992, pp. 883–886.
49. Sun, D.-Z. and Riedel, H., Prediction of shape distortions of hard metal parts by numerical simulation of pressing and sintering. In *Simulation of Materials Processing: Theory, Methods and Applications, Numiform 95*, ed. S.-F. Shen and P. R. Dawson. Balkema, Rotterdam, 1995, pp. 881–886.
50. McHugh, P. E. and Riedel, H., A liquid phase sintering model—application to Si_3N_4 and WC-Co. *Acta Metall. Mater*., 1997, **45**, 2995–3003.
51. Plankensteiner, A. F., Kraft, T. and Riedel, H., Micromechanism Based Macrostructural Finite Element Analysis of the Powder Metallurgical Process Route of Refractory Metals, In: *Fifth World Congress on Computational Mechanics*, WCCM V, (Ed.) H. A. Mang, F. G. Rammerstorfer and J. Eberhardsteiner, Vienna University of Technology, Austria. Available: http://wccm.tuwien.ac.at, 2002, (only on WWW).
52. Svoboda, J. and Riedel, H., New solutions describing the formation of interparticle necks in solid-state sintering. *Acta Metall. Mater*., 1995, **43**, 1–10.
53. Svoboda, J., Riedel, H. and Zipse, H., Equilibrium pore surfaces, sintering stresses and constitutive equations for the intermediate and late stages of sintering—Part I: computation of equilibrium surfaces. *Acta Metall. Mater*., 1994, **42**, 435–443.
54. Riedel, H., Zipse, H. and Svobada, J., Equilibrium pore surfaces, sintering stresses and constitutive equations for the intermediate and late stages of sintering—Part II: diffusional densification and creep. *Acta Metall. Mater*., 1994, **42**, 445–452.
55. Riedel, H., Kozák, V. and Svoboda, J., Densification and creep in the final stage of sintering. *Acta Metall. Mater*., 1994, **42**, 3093–3103.
56. Riedel, H., Svoboda, J. and Zipse, H., Numerical simulation of die pressing and sintering—development of constitutive equations. In *Powder Metallurgy World Congress PM94*, ed. D. Francois. Les Editions de Physique Les Ulis, Paris, 1994, pp. 663–671.
57. Svoboda, J. and Riedel, H., Quasi-equilibrium sintering for coupled grain boundary and surface diffusion. *Acta Metall. Mater*., 1995, **43**, 499–506.
58. Svoboda, J. and Riedel, H., Pore-boundary interactions and evolution equations for the porosity and the grain size during sintering,. *Acta Metall. Mater*., 1992, **40**, 2829–2840.
59. Riedel, H. and Svoboda, J., A theoretical study of grain coarsening in porous solids. *Acta Metall. Mater*., 1993, **41**, 1929–1936.
60. Riedel, H. and Blug, B., A Comprehensive model for solid state sintering and its application to silicon-carbide. In *Multiscale Deformation and Fracture in Materials and Structures: The J.R. Rice 60th Anniversary Volume, Solid Mechanics and Its Application, Vol. 84*, ed. T. J. Chuang and J. W. Rudnicki. Kluwer Academic Publishers, Dordrecht, 2001, pp. 49–70.
61. Kanters, J., Eisele, U. and Rödel, J., Scale dependent sintering trajectories. *Acta Mater*., 2000, **48**, 1239–1246.
62. Svoboda, J., Riedel, H. and Gaebel, R., A model for liquid phase sintering. *Acta. Metall. Mater*., 1996, **44**, 3215–3226.
63. Markondeya Raj, P., Odulena, A. and Cannon, W. R., Anisotropic shrinkage during sintering of particle-oriented systems—numerical simulation and experimental studies. *Acta Mater*., 2002, **50**, 2259–2570.
64. Ashby, M. F., *HIP 6.0 Background reading,* University of Cambridge, 1990.
65. Arzt, E., The influence of an increasing particle coordination on the densification of spherical powders. *Acta Metall*, 1982, **30**, 1883–1890.
66. Scherer, G. W., Sintering inhomogeneous glasses: application to optical waveguides. *J. Non-Crystalline Solids*, 1979, **34**, 239–256.
67. Jagota, A. and Dawson, P. R., Micromechanical modeling of powder compacts—unit problems for sintering and traction induced deformation. *Acta Metall*, 1988, **36**, 2551–2561 2563-2573.
68. McMeeking, R. M. and Kuhn, L. T., A diffusional creep law for powder compacts. *Acta Metall. Mater*., 1992, **40**, 961–969.

69. Burton, B., Interface reaction-controlled diffusional creep. A consideration of grain boundary dislocation climb sources. *Mater. Sci. Eng.*, 1972, **10**, 9–14.
70. Cocks, A. C. F., Interface reaction controlled creep. *Mech. Mater.*, 1992, **13**, 165–174.
71. Chuang, T.-J. and Rice, J. R., The shape of intergranular creep cracks growing by surface diffusion. *Acta Metall*, 1973, **21**, 1625–1628.
72. Chuang, T.-J., Kagawa, K. I., Rice, J. R. and Sills, L. B., Non-equilibrium models for diffusive cavitation of grain interfaces,. *Acta Metall*, 1979, **27**, 265–284.
73. Kucherenko, S., Pan, J. and Yeomans, J. A., A combined finite element and finite difference scheme for computer simulation of microstructure evolution and its application to pore-boundary separation during sintering. *Comp. Mater. Sci.*, 2000, **18**, 76–92.
74. Hillert, M., On the theory of normal and abnormal grain growth. *Acta Metall.*, 1965, **13**, 227–239.
75. Coube, O. and Riedel, H., Numerical simulation of metal powder die compaction with special consideration of cracking. *Powder Metall.*, 2000, **43**, 123–131.
76. Kraft, T., Riedel, H., Rosenfelder, O. and Stingl, P., Computational optimization of parts produced from ceramic powders. In *Microstructures, Mechanical Properties and Processes EUROMAT 1999, vol. 3*, ed. Y. Bréchet. Wiley-VCH, Weinheim, 2000, pp. 337–342.
77. Kraft, T., Riedel, H. and Rosenfelder, O., Modeling of powder die compaction and sintering of a disc seal. *Int. J. Powder Metall.* (submitted for publication).
78. Kraft, T., Optimising press tool shapes by numerical simulation of compaction and sintering-application to a hard metal cutting insert. *Modelling Simul. Mater. Sci. Eng.*, 2003, **11**, 381–400.
79. Riedel, H., A constitutive model for the finite-element simulation of sintering—distortions and stresses. In *Ceramic Powder Science III*, ed. G. L. Messing, S.-I. Hirano and H. Hausner. American Ceramic Society, Westerville, OH, 1990, pp. 619–630.